NUMERICAL MODELLING OF THE PUNCHING BEHAVIOUR OF STEEL FIBRE REINFORCED SELF-COMPACTING CONCRETE FLAT SLABS

BARROS, Joaquim A.O. [1], TEIXEIRA, Marcos D.E. [2], CUNHA, Vítor M.C.F. [3], Morais Neto, B.N. [4], VENTURA-GOUVEIA, António [5]

Abstract

Punching shear failure on flat reinforced concrete slabs of residential and commercial buildings is generally avoided by using transversal reinforcement and/or chapiters. The first option requires intense labour, mainly when densely flexural reinforcement exists in the potential punching failure region, with detrimental consequences in terms of costs of this construction solution. The second option has also extra costs due to the necessity of special arrangements of moulds for casting the chapiters. The interference of a chapiter on the flatness of the slab can also be a negative aspect from the architectonic point of view. The use of steel fibre reinforcement can be a solution to avoid both the conventional punching reinforcement and chapiters. Therefore, an experimental program was carried out to assess the potentialities of steel fibre reinforced self-compacting concrete (SFRSCC) for the punching resistance of flat slabs centrically loaded. This experimental program is described, and the main results are presented and analysed. To assess the potentialities of the Reissner-Mindlin FEM-based theory for modelling the behaviour of flat SFRSCC slabs submitted to punching loading configuration, new features were introduced in the out-of-plane shear constitutive law of the SFRSCC. These features are briefly described and the main focus was given on the modelling strategy adopted for simulating the punching tests.

Keywords: Flat Slab, SFRSCC, Punching Shear, Numerical Simulations

1. Introduction

The design of flat slabs is mostly governed by both serviceability conditions, namely quite high deflections in service, and ultimate limit states under punching shear [1, 2]. The

[1] BARROS Joaquim A.O., ISISE, Univ. Minho, Guimarães, Portugal, barros@civil.uminho.pt

[2] TEIXEIRA Marcos D.E., ISISE, Univ. Minho, Guimarães, Portugal, marcos.teixeira@civil.uminho.pt

[3] CUNHA Vítor M.C.F., ISISE, UTAD, Vila Real, Portugal, vcunha@utad.pt

[4] MORAIS NETO, Bernardo, University of Minho/University of Brasília-UnB, Dep. Civil Eng., School of Eng., Guimarães, Portugal, bnmn@hotmail.com

[5] VENTURA-GOUVEIA António, ISISE, Inst. Politécnico de Viseu, Viseu, Portugal, ventura@estgv.ipv.pt

adopted suspended flat slabs structural system (slabs supported on RC columns) might be prone to punching shear failure, as a consequence of the small slab thickness and absence of chapiters to ease up the transfer of forces from the slab to the column. Moreover, traditional stirrups as shear reinforcement are unsuitable for slabs with shallow depth less than 150 mm [3]. The adoption of a hybrid reinforcement solution (rebar + discrete fibres) in the slab/column connection might be a good reinforcing solution. The steel bars are used for the flexural reinforcement, while steel fibres guaranty the punching resistance [4] and improve the bond behaviour of steel bars. In fact, steel fibres are able of maintaining the structural integrity of the slab (or other member), thus avoiding the type of brittle collapse and damage usually observed in structural elements failing by punching shear [5, 6].

In this work the results of punching shear tests carried out on flat slabs with a hybrid reinforcement (rebar + discrete fibres) are presented and discussed. Four half scaled slabs, reinforced with distinct fibre contents, namely, 0, 60, 75 and 90 kg/m^3 were tested. The experimental results were numerically modelled under the finite element method (FEM) framework. Moreover, it is described the adopted multi-fixed smeared crack model within the Reissner-Mindlin theory, which is available in the FEMIX 4.0 software.

2. Punching shear test setup and results

2.1 Slab prototypes

The geometry of the type of slab of the experimental program is represented in Fig. 1. The load was applied in the centre of the slab by using a steel plate of 200×200×50 mm^3 placed in between the actuator and the slab.

The flexural reinforcement adopted in the reference slabs and in steel fibre reinforced self-compacting concrete (SFRSCC) slabs are represented in Fig. 2.a and 2.b, respectively. In these last ones, the reinforcement in the two directions is limited to a strip in the central zone with a width of about e+6d, where e is the edge of the loading steel plate, and d is the internal arm of the slab (Fig. 2.c). The reinforcement ratio, ρ, in the two main strips was 0.88%, and was equal in all the tested slabs.

During concrete casting the flexural reinforcement was in the top surface in order to reproduce, as closest as possible, the real conditions of a flat slab supported on columns in a building construction. This is an important aspect, since the content of steel fibres tends to increase from top to bottom due to the highest specific weight of the steel, and this is more pronounced when mechanical vibration is used during casting process [7, 8], leading, in general, to larger positive than negative resisting bending moments.

The concrete was prepared in a ready mix plant with an average compressive strength (f_{cm}) of 50 MPa at 28 days. Four slabs were casted, one without fibre reinforcement and three slabs with 60, 75 and 90 kg/m^3, respectively, of hooked ends steel fibres of 37 mm length (l_f), 0.55 mm diameter (d_f), 67 of aspect ratio (l_f/d_f), and tensile strength of about 1100 MPa. The full program is described in Tab. 1. The following acronym was used to designate the type of concrete applied in the experimental program: *CfXfcY*, where *X* is the aimed content of steel fibres in kg/m^3, and *Y* is the target average concrete compressive strength. For instance, *Cf75fc50* is the concrete reinforced with 75 kg/m^3 of fibres with a target f_{cm}=50MPa.

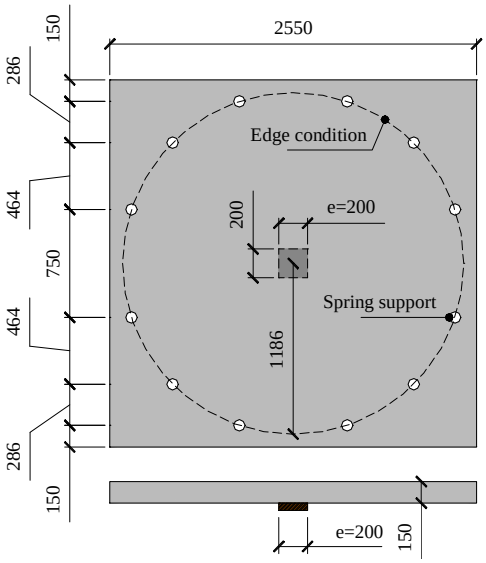

Fig. 1: Geometry of the slab prototype (dimensions in mm) [5]

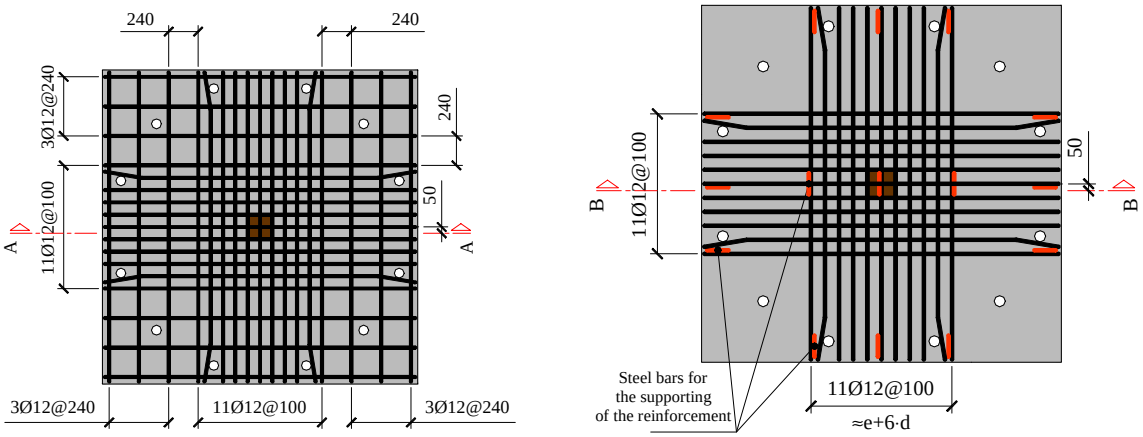

a) reference slabs b) SFRC slabs

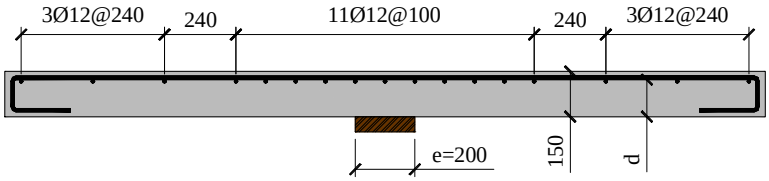

c) Cross section of AA

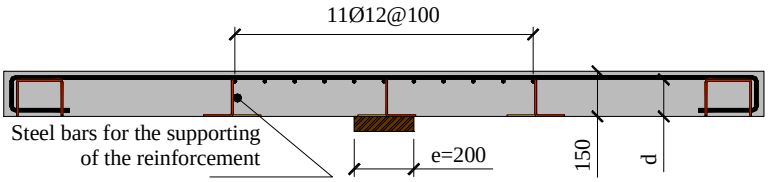

d) Cross section of BB

Fig. 2: Flexural reinforcement (dimensions in mm) [5]

After the punching tests have been executed, the internal arm of the flexural reinforcement, *d*, was measured in several cross sections, and the average value of *d* for each slab is indicated in Tab. 1. Difficulties were faced to assure a constant *d* in the slabs of the

experimental program, having d ranged between 117 and 133 mm. The ρ indicated in this table was determined by considering the d value measured experimentally.

Tab. 1: Characteristics of the experimental program

Series	d (mm)	ρ (%)	f_{cm} (MPa)	C_f (kg/m^3)
Cf0fc50	126	0.85	50	0
Cf60fc50	122	0.89	50	60
Cf75fc50	129	0.81	50	75
Cf90fc50	118	0.95	50	90

2.2 Test setup

Fig. 3 shows the test setup developed for the execution of the punching tests of the experimental program. An upward loading direction was applied by using an actuator of 1000 kN capacity with a load cell. Between the actuator and the bottom surface of the slab, in the central part of the slab, a steel plate with dimensions represented in Fig. 2 was used to distribute, as uniform as possible, the load applied by the actuator. Between the piston of the actuator and the steel plate, a metallic hinge was introduced to minimize the application of parasitic bending moments, and assure as much as possible double symmetry conditions for the test. The test was executed under displacement control, at a displacement rate of 0.05 mm/min in the centre point of the slab.

A slab was supported on twelve dywidag steel bars of 35 mm diameter. These twelve bars have passed through twelve holes of an average diameter of 60 mm executed after the concrete of the slab has been cured (Fig. 3.b). The inferior extremity of eight of these bars were pinnely connected to the reaction floor, while the superior extremity was fixed to the top surface of the slab by using steel plates of 200×200×50 mm^3. Due to restrictions on the pattern of the holes in the reaction slab, steel profiles were used to support four dywidag steel bars. Steel tubular tubes were also used to temporarily support the slab when installing the monitoring system.

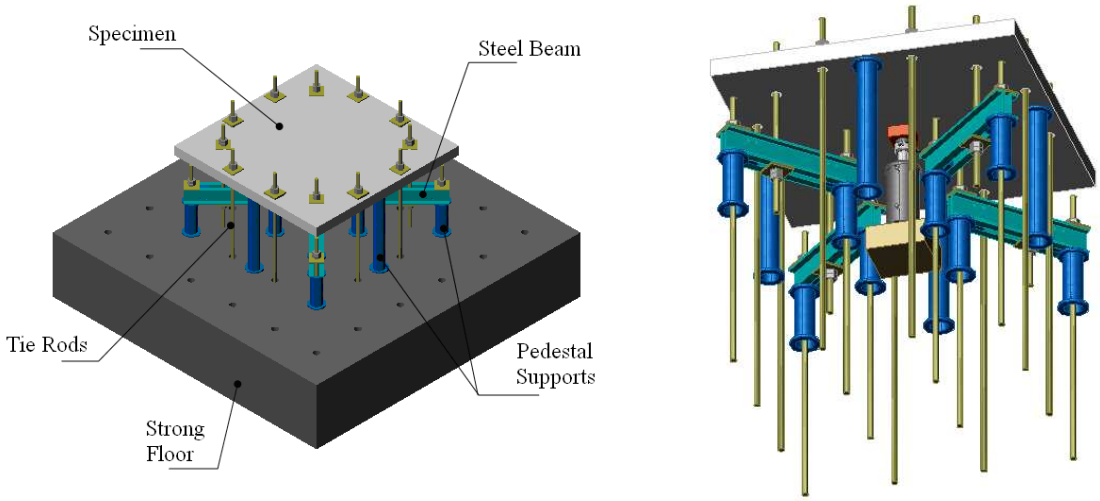

a) Top View b) Bottom View

Fig. 3: Test setup [5]

2.3 Materials and properties

2.3.1 Concrete

The mix compositions of the four slabs of the experimental program are indicated in Tab. **2**. The compositions for different content of fibres have some differences in order to take into account the interference of the fibres in the skeleton arrangement of the aggregates, by providing the best arrangement of the concrete constituents and assuring self-compactability requisites without occurrence of segregation for the constituents in all the mixes. By executing slump cone and Lbox tests it was obtained an average value of 615 mm for the spread diameter and a 0.9 for the H_2/H_1 blocking ratio parameter [9].

Tab. 2: Concrete compositions for the slabs of the experimental program (per m^3)

Series	Cement	Fly ash	Coarse aggregate (D_{max}=12 mm)	Coarse Sand	Fine sand	Super-plasticizer	Water	Fibres
Cf0fc50	420	65	670	806	269	6.79	165	0
Cf60fc50	420	65	668	804	268	7.76	165	60
Cf75fc50	420	75	661	795	265	7.92	168	75
Cf90fc50	420	80	657	790	265	8.00	170	90

For each slab, nine cylinders of 150 mm diameter and 300 mm height and nine beams of 150×150×600 mm^3 dimensions were cast and cured in the same conditions of the corresponding slab. The cylinder specimens were used to evaluate the average compressive strength f_{cm}, and the stress-strain response of concrete in compression [10]. The prismatic specimens were used to determine the flexural tensile strength of the developed concretes, and to evaluate the post-cracking residual strength parameters ($f_{R,j}$) of SFRC according to the recommendations of the CEB-FIP Model Code 2010 (2011) [11]. The $f_{R,i}$ can be used to define the constitutive law of the SFRC for design purposes, by using the recommendations of the CEB-FIP Model Code 2010 [11]. From each three notched beam bending test it was obtained a relationship between the applied force and the crack mouth opening displacement (CMOD). By evaluating the force at CMOD values of 0.5, 1.5, 2.5 and 3.5 mm, the $f_{R,j}$ values are determined by applying the following equation:

$$f_{r,j} = \frac{3F_j L}{2bh_{sp}^2} \quad (1)$$

where b=150 mm and L=500 mm are the width and the span of the specimen, and h_{sp} is the distance between the tip of the notch and the top of the cross section. In an attempt of assuring an unique crack progressing along the notched plane in the three point SFRC beam bending tests, the depth of the notch was increased with the content of fibres (25, 42.5 and 60 mm for the Cf = 60, 75 and 90 kg/m^3, respectively), as indicated in the second column of Tab. 4. Therefore, the h_{sp} for the specimens of the series Cf = 60, 75 and 90 kg/m^3 was 125, 107.5 and 90 mm, respectively.

By using the $f_{R,j}$ values, the CEB-FIP Model Code 2010 [11] propose the post-cracking residual strength obtained for an ultimate crack opening of w_u=1.5mm (f_{Ftu}) to be used in the design models:

$$f_{Ftu} = f_{Fts} - \frac{w_u}{2.5} \cdot (f_{Fts} - 0.5 \cdot f_{R3} + 0.2 \cdot f_{R1}) \geq 0\ ; \qquad f_{Fts} = 0.45 \cdot f_{R1} \qquad (2)$$

Tab. 3 presents the f_{cm} and the strain at peak compressive strength, ε_{cp}, recorded in the compressive tests according to the ISO 1920-3 [10]; the flexural tensile strength, $f_{fct,L}$, and the $f_{R,j}$ according to CEB-FIP Model Code 2010 [11]. Additionally, the obtained values for the f_{Ftu} are also indicated in Tab. 3.

Tab. 3: Average values of the compression and flexural tests

Series	Compression		Three point notched beam bending tests					
	$f_{cm,exp}$ (MPa)	$\varepsilon_{cp,exp}$ (‰)	$f_{fct,L}$ (MPa)	$f_{R,1}$ (MPa)	$f_{R,2}$ (MPa)	$f_{R,3}$ (MPa)	$f_{R,4}$ (MPa)	f_{Ftu} (MPa)
Cf0fc50	57.61 (0.90)	3.04 (2.65)	5.16 (6.71)	-	-	-	-	-
Cf60fc50	51.90 (6.49)	3.54 (1.83)	3.55 (10.77)	5.71 (20.93)	4.55 (19.50)	2.77 (21.79)	2.13 (29.86)	1.17
Cf75fc50	55.68 (3.91)	4.01 (7.02)	4.27 (5.97)	6.32 (23.89)	5.42 (18.07)	3.25 (23.01)	2.19 (31.48)	1.35
Cf90fc50	56.39 (4.38)	4.41 (11.78)	4.04 (9.93)	11.02 (15.36)	13.62 (16.29)	12.61 (21.08)	10.83 (25.29)	4.44

Values in round brackets: COV

Before commenting the results just presented, it should be mentioned that all the concrete compositions and casting procedures of the slabs and corresponding specimens were executed in a ready concrete company. The fibres were transported in a treadmill towards the mixer. After casting the *Cf60fc50* and *Cf75fc50* slabs it was verified that fibres had fallen down from the treadmill during the transportation procedure of the fibres to the mixer. Therefore, to estimate the content of fibres (C_f) really existing in the slabs and corresponding specimens, the number of fibres in the fracture surface (N_f) of the three point notched beam bending tests was evaluated according to the strategy described in [8]. Considering N_f, and following the approach proposed by [12], the obtained C_f for the tested slabs are presented in Tab. 4. It is verified that the content of fibres applied in the *Cf60fc50* and *Cf75fc50* compositions seems to have been much lower than the target value. This had a significant impact on the test results with notched beams and punching slabs, in a consistent manner.

Tab. 4: Content of fibres in the notched plane of SFRC beam bending tests, and the theoretical content of fibres

Series	Depth of the notched cross section (mm)	Nº of fibres (N_f)	Fibres per unit area (cm^2)	Theoretical estimation of the content of fibres (kg/m^3)
Cf60fc50	125	166	0.89	30
Cf75fc50	107.5	155	0.96	32
Cf90fc50	90	305	2.26	76

The average value of the f_{cm} was 55.4 MPa (with a COV of about 5%), a little bit higher than the aimed value. The number of fibres in the notched fracture surface of the tested specimens, and the corresponding theoretical content of fibres, included in Tab. 4, clearly support the tendency obtained in the results in the notched beam bending tests presented in Tab. 3. In fact the $f_{R,j}$ follow closely the C_f obtained.

2.3.2 Steel bars

Five steel bar specimens representative of the conventional flexural reinforcement were submitted to uniaxial tensile tests according to the recommendations of ISO 15630-1 [13]. The average values of the obtained results are indicated in Tab. 5, where ε_{sy} and f_{sy} are the strain at yield initiation and the corresponding stress, ε_{su} is the strain at maximum tensile stress, f_{su}, and E_s is the elasticity modulus.

Tab. 5: Average values of the tensile properties of the steel bars forming the flexural reinforcement of the slabs

Diameter (mm)	ε_{sy} (‰)	f_{sy} (MPa)	ε_{su} (‰)	f_{su} (MPa)	E_s (GPa)
12	2.53	530	-	684	209.49

3. Results and discussion

3.1 Load-deflection response

Fig. 4 represents the load versus deflection in the centre of the tested slabs. Tab. 6 includes the relevant obtained results, where P_{max} is the maximum applied load, and δ_{Pmax} is its corresponding deflection, P_{max}^{SFRC} and P_{max}^{REF} are the maximum load of the SFRC slab and its corresponding reference slab, $\delta_{P_{max}}^{SFRC}$ and $\delta_{P_{max}}^{REF}$ are the deflection at P_{max} of a SFRC slab and its corresponding reference slab. This table also includes the failure mode observed in each slab.

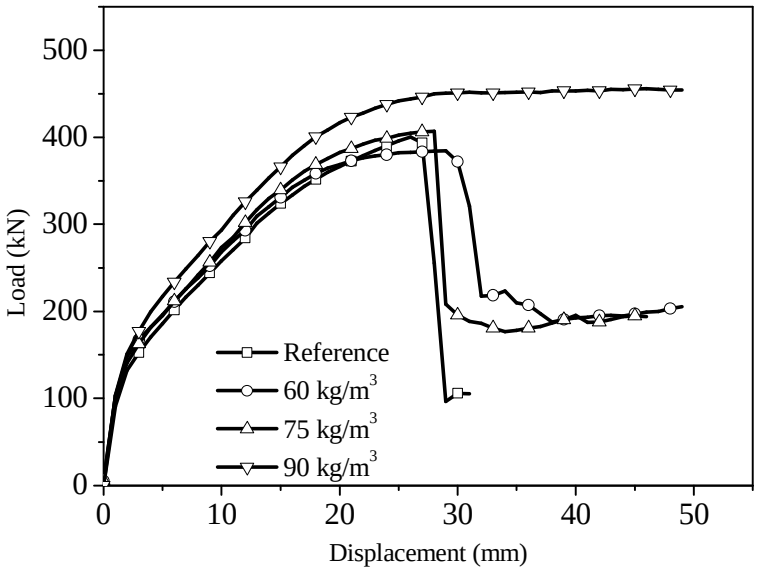

Fig. 4: Load versus centre deflection in the tested series

The following results show a clear tendency of an increase of the load carrying capacity of the slabs with the increase of $f_{R,i}$. These results evidence that the properties at the material level, such is the case of the number of fibres in the fracture surface of the notched beam bending tests, the corresponding post-cracking residual strength parameters provide good indicators in terms of slab's load carrying capacity, since a linear trend between these parameters is observed.

Tab. 6: Main results obtained in the punching tests

Slab	P_{max} **(kN)**	δ_{Pmax} **(mm)**	$\frac{P_{\max}^{SFRC}}{P_{\max}^{REF}}$	$\frac{\delta_{\max}^{SFRC}}{\delta_{\max}^{REF}}$	**Failure mode**
Cf0fc50	409.11	26.58	-	-	Punching
Cf60fc50	386.08	28.23	0.94	1.06	Punching
Cf75fc50	408.03	27.56	1.00	1.04	Punching
Cf90fc50	456.53	45.81	1.12	1.72	Bending

Due to the relative low content of fibres really introduced in the *Cf60fc50* and *Cf75fc50* slabs (around 30 kg/m^3 – see Tab. 4), they have failed in punching like the corresponding reference slabs (see Tab. 6). This can be supported on the relatively low values obtained for f_{Ftu} for these slabs (Tab. 3).

The results in Tab. 6 show that the increase in terms of maximum load was only significant (12%) in the *Cf90fc50* that has failed in bending. Tab. 1 shows that the internal arm (*d*) of the conventional flexural reinforcement of the *Cf90fc50* slab was significantly smaller than the *d* of the corresponding reference slabs. Therefore, if in the SFRC slabs it has been assured values of *d* equal to the corresponding reference slabs, a higher increase of $P_{max}^{SFRC}/P_{max}^{REF}$ would have been obtained for the SFRC slabs.

In terms of deflection at maximum load, $\delta_{P_{max}}$, the increase of the $\delta_{max}^{SFRC}/\delta_{max}^{REF}$ ratio, as expected, was only significant in the slabs failing in bending (Tab. 6), with an increase of 72% in *Cf90fc50* slab. The relatively low content of fibres really introduced in the *Cf60fc50* and *Cf75fc50* slabs (about 30 kg/m^3) has only contributed for an increase of the deflection at punching failure load (4 to 6%).

4. Numerical model

To simulate the material nonlinear behaviour of thin fibre reinforced concrete (FRC) structures, where out-of-plane shear deformation might be appreciable, the Reissner-Mindlin theory was selected [14]. The damage due to crack formation and propagation was simulated by discretizing the thickness of the shell in several layers. Fibres bridging micro-cracks contribute to the formation of diffuse crack patterns, since they offer resistance to the degeneration of these micro-cracks into macro-cracks. Therefore, smeared crack constitutive models are, conceptually, more appropriate than discrete crack models in the simulation of crack propagation in FRC structures, mainly in those with a great number of redundant supports [15]. Due to the lack of space, the present paper only describes the innovative aspects introduced in the multi-fixed smeared crack

model in order to attempt the caption of the punching failure mode. This model is available in the FEMIX 4.0 computer program, and its full description can be found elsewhere [16].

For the case of cracked concrete the constitutive law is defined by the following Equation.

$$\begin{bmatrix} \Delta\underline{\sigma}_{mf} \\ \underline{\sigma}_s \end{bmatrix} = \begin{bmatrix} \underline{D}_{mf}^{crco} & \underline{0} \\ \underline{0} & \underline{D}_s^{crco} \end{bmatrix} \begin{bmatrix} \Delta\underline{\varepsilon}_{mf} \\ \underline{\varepsilon}_s \end{bmatrix} \tag{3}$$

where $\Delta\underline{\sigma}_{mf}$ and $\Delta\underline{\varepsilon}_{mf}$ are the vectors corresponding to the in-plane stress and strain increment components (membrane and bending), and $\underline{\sigma}_s$ and $\underline{\varepsilon}_s$ are the vectors corresponding to the out-of-plane shear stress and shear strain components, respectively. In Eq. (3) $\underline{D}_{mf}^{crco}$ is the in-plane cracked concrete constitutive matrix [16]:

$$\underline{D}_{mf}^{crco} = \underline{D}_{mf,e}^{co} - \underline{D}_{mf,e}^{co}\left[\underline{T}^{cr}\right]^T \left(\underline{D}^{cr} + \underline{T}^{cr}\underline{D}_{mf,e}^{co}\left[\underline{T}^{cr}\right]^T\right)^{-1} \underline{T}^{cr}\underline{D}_{mf,e}^{co} \tag{4}$$

where $\underline{D}_{mf,e}^{co}$ is the constitutive matrix for linear-elastic concrete, $\underline{T}^{cr}$ represents the transformation matrix from the crack local coordinate system to the element local coordinate system and $\underline{D}^{cr}$ is the crack constitutive matrix:

$$\underline{D}^{cr} = \begin{bmatrix} D_I^{cr} & 0 \\ 0 & D_{II}^{cr} \end{bmatrix} \tag{5}$$

In this equation, D_I^{cr} and D_{II}^{cr} represent, respectively, the constitutive components corresponding to the crack opening mode I (normal) and crack sliding mode II (in-plane shear). The fracture mode I modulus, D_I^{cr}, is defined in Fig. 5, where α_i and ξ_i are the parameters that define the shape of the crack normal stress vs. crack normal strain diagram. The ultimate crack strain ($\varepsilon_{n,u}^{cr}$) is defined as a function of α_i and ξ_i parameters, of fracture energy (G_f^I), tensile strength ($f_{ct} = \sigma_{n,1}^{cr}$) and crack bandwidth ($l_b$), as follows [16],

$$\varepsilon_{n,u}^{cr} = \frac{2}{\xi_1 + \alpha_1\xi_2 - \alpha_2\xi_1 + \alpha_2} \cdot \frac{G_f^I}{f_{ct} l_b} \tag{6}$$

The fracture mode II modulus, D_{II}^{cr}, is obtained from,

$$D_{II}^{cr} = \frac{\beta}{1-\beta} G_c \tag{7}$$

with

$$\beta = \left(1 - \frac{\varepsilon_n^{cr}}{\varepsilon_{n,u}^{cr}}\right)^{p_1} \tag{8}$$

where β is the shear retention factor, defined as a constant value or as a function of the actual crack normal strain (ε_n^{cr}) and the ultimate crack normal strain ($\varepsilon_{n,u}^{cr}$), and G_c is the concrete elastic shear modulus. When a linear decrease of β with the increase of ε_n^{cr} is assumed, then $p_1 = 1$. Larger values of the exponent p_1 correspond to a faster decrease of the parameter β [16]. The use of a softening constitutive law to model the in-plane crack shear stress transfer can improve the accuracy of the simulation of structures failing in shear [17]. However, the simultaneous presence of softening laws to model fracture modes I and II introduces additional difficulties on assuring convergence during the loading procedure of a material nonlinear analysis.

The diagram represented in Fig. 6 was used to simulate the out-of-plane constitutive matrix, $\underline{D}_s^{crco}$. When the portion of concrete associated with the IP changes from

uncracked to cracked state, the out-of-plane shear stresses are stored and the relation between each out-of-plane shear stress-strain ($\tau_{23} - \gamma_{23}$ and $\tau_{31} - \gamma_{31}$) follows the softening depicted in Fig. 6. Therefore, the matrix $\underline{D}_s^{crco}$ in Eq. (3) is defined by

$$\underline{D}_s^{crco} = \begin{bmatrix} D_{III,sec}^{23} & 0 \\ 0 & D_{III,sec}^{31} \end{bmatrix} \tag{9}$$

where

$$D_{III,sec}^{23} = \frac{\tau_{23,max}^{OP}}{\gamma_{23,max}^{OP}};\ D_{III,sec}^{31} = \frac{\tau_{31,max}^{OP}}{\gamma_{31,max}^{OP}} \tag{10}$$

according to a secant approach (see Fig. 6).

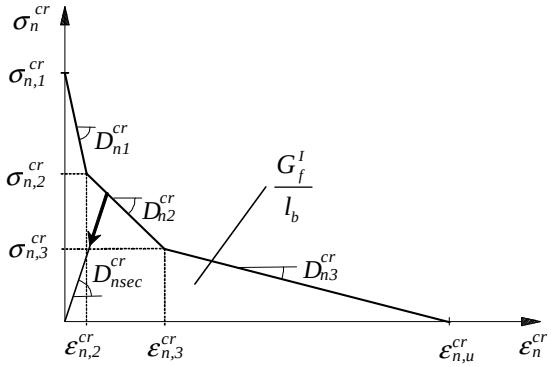

Fig. 5: Trilinear stress-strain diagram for modelling the fracture mode I ($\alpha_1 = \sigma_{n,2}^{cr}/\sigma_{n,1}^{cr}$, $\alpha_2 = \sigma_{n,3}^{cr}/\sigma_{n,1}^{cr}$, $\xi_1 = \varepsilon_{n,2}^{cr}/\varepsilon_{n,u}^{cr}$ and $\xi_2 = \varepsilon_{n,3}^{cr}/\varepsilon_{n,u}^{cr}$)

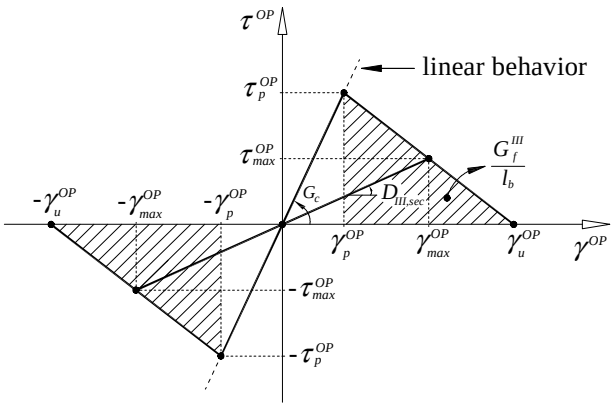

Fig. 6: Generic out-of-plane (OP) shear stress-strain diagram

For each out-of-plane shear component, the peak shear strain is calculated using both the stored peak shear stress at crack initiation and G_c:

$$\gamma_{23,P}^{OP} = \frac{\tau_{23,p}^{OP}}{G_c};\ \gamma_{31,P}^{OP} = \frac{\tau_{31,p}^{OP}}{G_c} \tag{11}$$

Each out-of-plane ultimate shear strain is defined as a function of the out-of-plane peak shear strain (γ_p^{OP}), the out-of-plane shear strength (τ_p^{OP}), the mode III (out-of-plane) fracture energy (G_f^{III}) and the crack bandwidth (l_b), as follows:

$$\gamma_{23,u}^{OP} = \gamma_{23,P}^{OP} + \frac{2G_f^{III}}{\tau_{23,p}^{OP}\, l_b};\ \gamma_{31,u}^{OP} = \gamma_{31,P}^{OP} + \frac{2G_f^{III}}{\tau_{31,p}^{OP}\, l_b} \tag{12}$$

In the present approach it is assumed that the crack bandwidth used for assuring mesh independence when modelling fracture mode I can also be used to define the dissipated energy in the out-of-plane fracture process.

5. Numerical simulations of the punching tests

5.1 Two-dimensional layered geometrical model

To simulate the punching shear slab tests, only one quarter of the slab was modelled, due to its double symmetry. In Fig. 7, the supports represented by a red square are related to the experimental support conditions. These three supports have only one fixed degree of freedom, in the *zz* direction, *i.e.* perpendicular to the *xy* plane. On the other hand, the blue circles correspond to the supports introduced to enforce the double symmetry condition. The load was applied at the bottom left corner of the mesh, *i.e.* centre point of the slab, under displacement control by the arc-length method. Further details of the adopted arc-length technique can be found elsewhere [18].

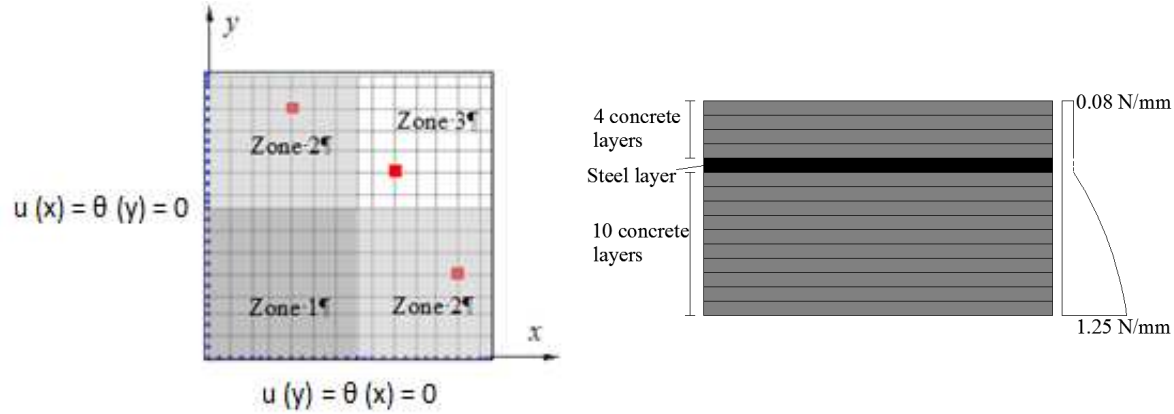

a) b)

Fig. 7: a) Mesh, supports and symmetry conditions adopted; b) Layer discretization of the slab's cross section

The adopted mesh is comprised by 196 Reissner-Mindlin shell elements (Fig. 7). A Gauss-Legendre integration scheme of 2×2 was adopted. Moreover, two distinct cracks can arise at each integration point. Each shell element was discretized into fifteen layers with a total depth of 150 mm. Within these layers, one is used to model the steel bars nonlinear behaviour, whereas the other ones are used to model the fracture process of the SFRSCC, namely, four for the cover concrete on the top of the slabs and ten for remaining concrete under the steel rebars. In Fig. 2, it is possible to notice that there are three zones of distinct longitudinal reinforcement ratios. These three zones were taken into account in the numerical model by adopting a distinct layer discretization for each zone (Fig. 7.a). Thus, Zone 1 is the one with the highest level of reinforcement, at the centre of the slab; Zone 2 is the one of intermediate level of reinforcement; and the Zone 3 presents the lower level of reinforcement. Note that in Zone 3, for the SFRSCC slabs, there is no conventional reinforcement, so there are 15 layers with the same thickness, 10 mm. Tab. 7 includes both the thickness and corresponding number of layers in each shell element at the distinct zones. The layers are enumerated in the positive direction of *z* axis.

Tab. 7: Thicknesses of the layers in the shell element (mm)

Slab	Zone	Concrete		Steel		Cover Concrete	
		Layer	Thick	Layer	Thick	Layer	Thick
Reference	1	[1-10]	12.238	11	1.244	[12-15]	6.595
	2	[1-10]	12.265	11	0.693	[12-15]	6.664
	3	[1-10]	12.293	11	0.141	[12-15]	6.733
SFRSCC	1	[1-10]	12.238	11	1.244	[12-15]	6.595
	2	[1-10]	12.269	11	0.622	[12-15]	6.672
	3	[1-15] 10.000					

5.2 Parameters for the constitutive material behaviour

The properties of the steel were directly obtained from the tensile tests performed on the steel bars, which were previously presented. The tensile behaviour of the steel was modelled with a quadrilinear relationship, similar to the one presented in Fig. 5. However the post-peak parameters translate the steel behaviour in the yielding stage. The parameters for the quadrilinear diagram are presented in Tab. 8. Note that G_f is a fictitious parameter that represents the energy dissipated by the steel. Moreover, for the Poisson's ratio (ν) was adopted a null value, 209.49 GPa for the Young modulus and 467.01 MPa for the compressive and tensile yielding stress.

Tab. 8: Parameters used to define the steel bar quadrilinear tensile law

$\sigma_{n,1}^{cr}$ (MPa)	$\sigma_{n,2}^{cr}$ (MPa)	$\sigma_{n,3}^{cr}$ (MPa)	$\sigma_{n,4}^{cr}$ (MPa)	$\varepsilon_{n,2}^{cr}$ (‰)	$\varepsilon_{n,3}^{cr}$ (‰)	$\varepsilon_{n,4}^{cr}$ (‰)	Gf (N/mm)
467.01	511.99	531.39	584	0.72	1.84	7.74	390.30

For the concrete bulk, the parameters used to define the constitutive post-cracking law depicted in Fig. 5 are presented in Tab. 9. For the elastic properties, a Poisson's ratio of 0.15 and a Young modulus of 37.20 GPa were adopted. The post-cracking behaviour considered for the *Cf0fc50* series was obtained according to the proposed by the CEB-FIP Model Code 2010 [11] for plain concrete. On the other hand, the parameters used for the post-cracking behaviour of the series with SFRSCC have been obtained by retrofitting the numerical response to the corresponding experimental one.

It is also important to refer that both the slabs *Cf60fc50* and *Cf75fc50*, the concrete layers are ascribed with distinct post-cracking behaviour as resumed in Tab. 9. As previously detailed in section 2.3.1, this slab had some issues during its casting, in particular with the effective fibre content. Therefore, to take into account a heterogeneous fibre distribution along the slab's depth, which could be ascribed to fibre segregation problems, distinct values for the fracture energy were attributed to the layers. The fracture energy decreased from 1.25 to 0.08 N/mm following up a parabolic trend from the bottom layer, layer n. 1 (compressed zone) to the top layer, layer n. 15 (tensioned zone), respectively (Fig 7.b and

Tab. 9). Since the real fibre content and average compressive strength of *Cf75fc50* slab were similar to those of *Cf60fc50* slab, the same values for the constitutive model were adopted in the simulation of these two slabs.

Tab. 9: Parameters of the post-cracking trilinear relationship for the concrete bulk

Series	**Layer**	**ξ_1 (-)**	**ξ_2 (-)**	**α_1 (-)**	**α_2 (-)**	**G_f (N/mm)**
Cf0fc50	-	0.100	0.999	0.095	0.00	0.08
Cf60fc50	[1-10]	0.033	0.250	0.250	0.250	[1.25 - 0.16]
Cf75fc50	[12-15]					0.08
Cf90fc50	-	0.005	0.100	0.300	0.200	3.50

5.3 Comparison of the numerical and experimental results

Fig. 8 depicts, for each slab, both the numerical and experimental curves.

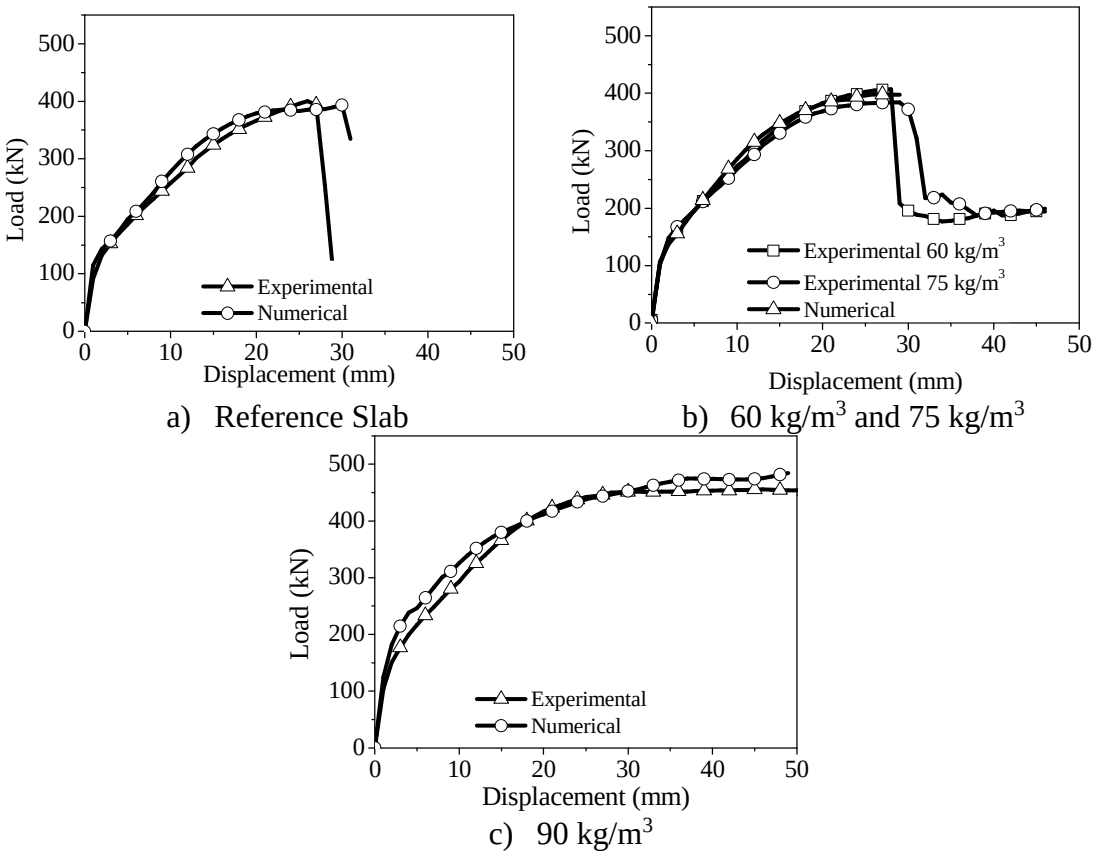

a) Reference Slab b) 60 kg/m^3 and 75 kg/m^3

c) 90 kg/m^3

Fig. 8: Experimental and numerical results

In general, it is possible to notice that the numerical simulations are in good accordance with the experimental curves. Concerning the numerical simulation of the *Cf0fc50* slab (Fig. 8.a), it was predicted the punching shear failure, however the displacement for which this type of failure occurs was slight overestimated, approximately 10%. On the other hand, for the *Cf60fc50* and *Cf75fc50* series (Fig. 8.b) the load decay observed experimentally due to punching was not captured experimentally due to difficulties on the convergence process of the numerical simulations of both slabs. However, the

deformational response was predicted with high accuracy, and since convergence was not possible to assure precisely at the deflection level coinciding with the punching failure observed experimentally it is presumed that the model is almost in the situation of capturing this type of failure mode. Finally, in the *Cf90fc50* series (Fig. 8.d), both the experimental and numerical curves are almost coincident in all their length. Neither of them shows a punching failure, due to the high fibre content used in this series.

6. Conclusions

In this work the results of punching shear tests carried out on flat slabs with a hybrid reinforcement (rebar + discrete fibres) are presented and discussed. Four half scaled slabs, reinforced with distinct fibre contents, namely, 0, 60, 75 and 90 kg/m^3 were tested. The experimental results were numerically modelled under the FEM framework. Moreover, it is described the adopted multi-fixed smeared crack model within the Reissner-Mindlin theory, which is implemented in the FEMIX 4.0 software.

Regarding the experimental results, a clear tendency of an increase of the load carrying capacity of the slabs with the increase of $f_{R,I}$ obtained from three-point bending tests was observed. This evidences that the corresponding post-cracking residual strength parameters provide good indicators in terms of slab's load carrying capacity, since a linear trend between these parameters is observed. Due to deficiencies on the automatic process of introducing the fibres into the mixer, the slabs reinforced with 60 and 75 kg/m^3 shown relative low content of fibres (around 30 kg/m^3). Therefore, both of them have failed in punching like the corresponding reference slabs. This can be supported on the relatively low values obtained for f_{Ftu} for these slabs. For the slab reinforced with 90 kg/m^3, an increase of 12% in terms of maximum load was observed, and a flexure failure mode was occurred.

The load-deflection curves obtained in the numerical simulations are in good accordance with the experimental ones. Moreover, the type of failure mode observed on the experimental tests was also successfully predicted.

Acknowledgements

This work is supported by FEDER funds through the Operational Program for Competitiveness Factors – COMPETE and National Funds through FCT – Portuguese Foundation for Science and Technology under the project "SlabSys - HFRC" PTDC/ECM/120394/2010.

References

[1] Chairlady, T.C., Vandewalle L., Leuven, K.U., "Design of steel fibre reinforced concrete using the σ-w method: Principles and applications", Materials and Structures/Materiaux et Constructions, 34(249) pp. 262-278, 2002.

[2] Muttoni A., "Punching Shear Strength of Reinforced Concrete Slabs without Transverse Reinforcement", ACI Structural Journal, 105(4) pp. 440-450, 2008.

[3] Choi KK, et. al., “Punching shear strength of interior concrete slab–column connections reinforced with steel fibers” Cement and Concrete Composites, pp. 409-420, 2007.

[4] Moraes-Neto, B.N.; Barros, J.A.O.; Melo, G.S.S.A., “A model for the prediction of the punching resistance of steel fibre reinforced concrete slabs centrically loaded”, Building Materials Journal, 46, pp. 211-223, 2013.

[5] Morais-Neto, B.N.,“Comportamento à Punção de Lajes Lisas em Concreto Reforçado com Fibras de Aço sob Carregamento Simétrico (Punching Behaviour of Steel Fibre Reinforced Self-compacting Concrete Flat Slabs under a Symmetric Loading)”, PhD Thesis, University of Brasília, Brazil [in Portuguese], 2013.

[6] Swamy R.N., “FRC for sustainable infrastructure regeneration and rehabilitation”, In Fibre-Reinforced Concretes (FRC) BEFIB 2000, pp. 3-18, Lyon, France, 2000.

[7] Alves, N.; Barros, J.A.O.; Nunes, Â; Lourenço, L.A.P., “Steel fibre reinforced self-compacting concrete for grid foundations of single-family houses”, 8th RILEM International Symposium on Fibre Reinforced Concrete: challenges and opportunities, Eds: Joaquim Barros et al., 12 pp., 19-21, September 2012.

[8] Barros, J.A.O.; Antunes, J.A.B., “Experimental characterization of the flexural behaviour of steel fibre reinforced concrete according to RILEM TC 162-TDF recommendations”, RILEM TC 162 TDF Workshop, pp. 77-89, 20-21, March 2003.

[9] EFNARC, “Specification and Guidelines for Self-Compacting Concrete”, ISBN, 0 9539733 4 4, 32 pp., 2002.

[10] ISO 1920-3. “Testing of concrete – Part 3: Making and curing test specimens” International Standard, First edition, October 2004.

[11] CEB-FIB Model Code 2010 “CEB-FIB Model Code 2010 – Final draft”, Thomas Thelford, Lausanne, Switzerland (2010).

[12] Abrishambaf, A.; Barros, J.A.O.; Cunha, V. M. C. F., “State of Art: Fibre Orientation and Dispersion”, Technical Report No. 11-DEC/E-30, University of Minho, 22 pp., April 2011.

[13] ISO 15630-1. “Steel for the reinforcement and prestressing of concrete - Test methods -Part 1: Reinforcing bars, wire rod and wire” International Standard, First edition, April 2002.

[14] Reissner, E., “The effect of transverse shear deformation on the bending elastic plates“, Jour. Appl. Mech., 12, pp. 69-76, 1945.

[15] Barros, J.A.O.; Figueiras, J.A. “Nonlinear analysis of steel fibre reinforced concrete slabs on grade”, Computers & Structures Journal, 79(1), pp. 97-106, January 2001.

[16] Ventura-Gouveia, A., “Constitutive models for the material nonlinear analysis of concrete structures including time dependent effects”, PhD Thesis, Department of Civil Engineering, University of Minho, 2011.

[17] Rots, J.G. and de Borst, R., “Analysis of mixed-mode fracture in concrete”, Journal of Engineering Mechanics, ASCE, 113(11), pp. 1739-1758, 1987.